

pubs.acs.org/NanoLett Letter

Mechanism of Extreme Optical Nonlinearities in Spiral WS₂ above the Bandgap

Xiaopeng Fan, [⊥] Zhurun Ji, [⊥] Ruixiang Fei, Weihao Zheng, Wenjing Liu, Xiaoli Zhu, Shula Chen, Li Yang, Hongjun Liu, Anlian Pan, * and Ritesh Agarwal*



Cite This: Nano Lett. 2020, 20, 2667-2673



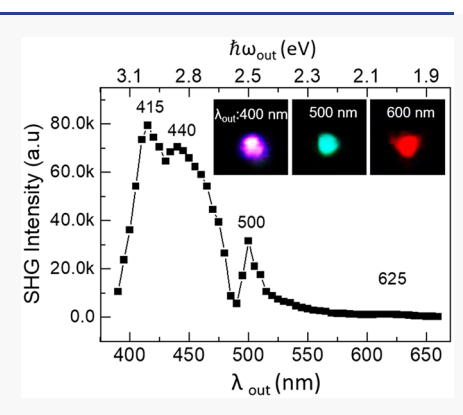
ACCESS

III Metrics & More

Article Recommendations

Supporting Information

ABSTRACT: Layered two-dimensional transition-metal dichalcogenides (2D-TMDs) are promising building blocks for ultracompact optoelectronic applications. Recently, a strong second harmonic generation (SHG) was observed in spiral stacked TMD nanostructures which was explained by its low crystal symmetry. However, the relationship between the efficiency of SHG signals and the electronic band structure remains unclear. Here, we show that the SHG signal in spiral WS₂ nanostructures is strongly enhanced (~100 fold increase) not only when the second harmonic signal is in resonance with the exciton states but also when the excitation energy is slightly above the electronic band gap, which we attribute to a large interband Berry connection associated with certain optical transitions in spiral WS₂. The giant SHG enhancement observed and explained in this study could promote the understanding and utility of TMDs as highly efficient nonlinear optical materials and potentially lead to a new pathway to fabricate more efficient optical energy conversion devices.



KEYWORDS: transition-metal dichalcogenides, two-dimensional materials, spiral nanostructure, second harmonic generation, exciton, Berry connection

ptical second harmonic generation (SHG) was discovered over 50 years ago and has been used as a ubiquitous tool in microscopic and spectroscopic techniques. 1-4 Modern integrated photonic circuits require high-efficiency nonlinear media to modulate photonic signals, but the efficiency of SHG has always been limited by the strict phase matching requirements in traditional nonlinear crystals.⁵ Nevertheless, when the crystal thickness is far below the coherence length of light, the phase matching requirements are relaxed.^{6,7} The emergence of two-dimensional (2D) van der Waals (vdW) nanostructures with broken inversion symmetry brought about many candidate materials for nonlinear nanocrystals. Due to the unique properties of layered transition-metal dichalcogenides (TMDs), such as MoS2, WS2, MoSe2, and WSe2, their linear and nonlinear optical properties have been widely explored.⁸⁻¹⁴ In particular, the SHG from monolayer TMDs has been studied both experimentally and theoretically. 10,15-18 However, the atomic thickness of monolayers constrains the amplitude of nonlinear optical signals, which is proportional to the square of the effective propagation distance, so an inversion symmetry broken multilayer TMD flake where the SHG signal can be enhanced would be the most suitable system for this propose. The Bernal stacked (2H) TMDs do not meet this requirement in spite of their thickness, since SHG is forbidden by inversion symmetry, and hence, only their top layers can contribute to the total signal intensity. 19,20 Different ways of breaking inversion symmetry in 2H-TMDs include special

stackings (artificial stackings or 3R stacking) and electric field biasing, ^{14,16,21,22} but these methods involve challenging physical manipulation of the system and have many restrictions. In addition to these, a spiral structure formed by natural screw-dislocation-driven (SDD) mechanism with a naturally broken inversion symmetry, showing an increasing SHG susceptibility with the increase of layer number compared to monolayer and few-layer structures, is quite promising. ^{13,23,24}

To improve the conversion efficiency of nonlinear optical signals in newly discovered materials, it is important to understand and utilize their inherent electronic properties. Recently, a strong nonlinear optical response of monolayer WSe₂ with resonance peaks ranging from 1.75 to 2.35 eV were observed at $T=4~\rm K.^{25}$ Also, resonance enhancements of monolayer and trilayer MoS₂ originating from the increased density of states at the Γ point was studied. However, these studies were based on few-layer TMDs, and hence, the SHG amplitudes even at excitonic resonances were quite weak. To achieve a higher conversion efficiency from TMDs, a

Received: January 22, 2020
Revised: February 27, 2020
Published: March 5, 2020





comprehensive study of SHG signals over a wide spectral range and their physical origins in spiral structures would be crucial. Here, we report an unusual variation of SHG signals over several orders of magnitude in the spectral range slightly above the estimated optical bandgap of WS₂ (estimated to be ~2.7 eV). Four significant enhancement peaks of emitted SHG intensity were observed, with the peak positions corresponding to the A, B, C, and D excitonic resonances as confirmed by the linear reflectance spectra. Besides excitonic properties, the features slightly above the C and D exciton peaks were attributed to the interband Berry connection near the Γ –K line in the Brillouin zone. ^{27,28} Our findings show the interplay between electronic properties and nonlinear optical susceptibility in TMDs and are promising for high-efficiency, compact nonlinear optical devices.

The spiral WS_2 flakes were grown by chemical vapor deposition (CVD) method^{29–31} on SiO_2/Si substrates and then transferred onto quartz substrates for optical measurements. For nonlinear optical measurements, a Ti/sapphire femtosecond laser combined with a confocal optical microscope was used, and SHG signals were collected in the transmission (Figure 1a, see Methods for details). The optical

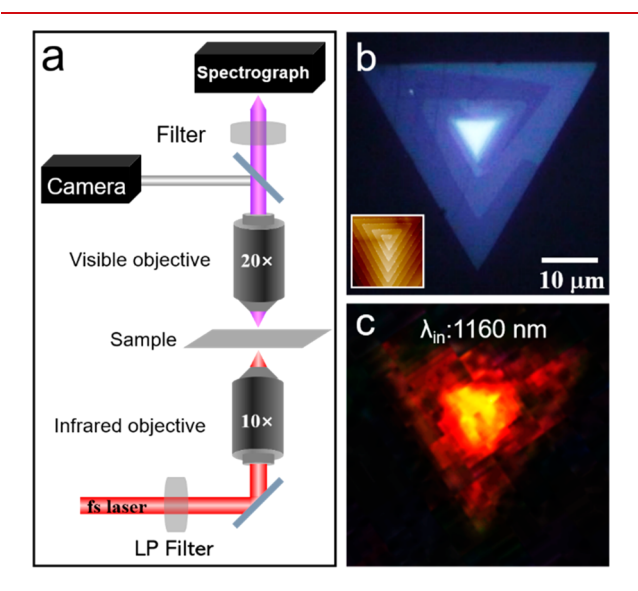


Figure 1. Schematic diagram of the optical setup and optical images of spiral WS₂. (a) Schematic diagram of our transmission mode nonlinear optical measurement system. (b) Optical and atomic force microscope (AFM) images of a single spiral WS₂ flake on the quartz substrate. Inset is the AFM image of single spiral WS₂ flake. (c) Charge-coupled device (CCD) image of the spiral WS₂ flake illuminated by the femtosecond laser with 1160 nm excitation wavelength (λ_{in}).

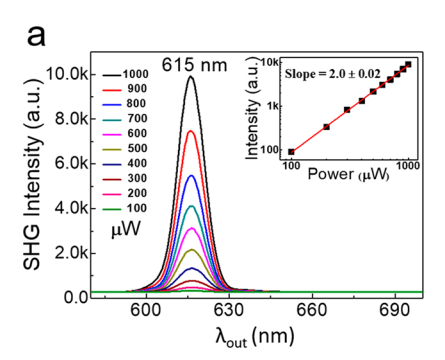
image in Figure 1b combined with the atomic force microscope (AFM) image (inset) show the structural characteristics of the spiral WS₂ where the spiral pattern starts from a single screw dislocation, and the total thickness at the center is ~20 nm (see Figure S1). Figure 1c shows the spatial distribution of the SHG intensity on the same flake with the laser spot size larger than the whole flake area. It can be seen that the emission energy $\hbar\omega_{\rm out}$ intensity increases with increasing layer numbers in the spiral structure, confirming that the spiral structure lacks inversion symmetry everywhere, and the contribution from each layer interferes constructively,

which differs from multilayer WS₂ flakes with regular 2H stacking, as discussed in our previous reports.^{23,24}

The second harmonic nature of the obtained signal was confirmed by the quadratic dependence of the emitted intensity with the laser power, as shown in Figure 2a. The excitonic states of spiral WS2 were then studied by the linear reflectance measurement, showing four peak positions corresponding to A, B, C, and D excitons at ~640, 530, 470, and 430 nm, respectively (Figure 2b). Also, the reflectance spectra measured at spots with different layer numbers displayed similar shapes with the excitonic peaks well matched and in correspondence with previous reports on WS2 monolayers. 19,32 This result is different from the Bernal stacked multilayer WS2, 33 because the four exciton-related peak positions and the photoluminescence (PL) peak positions (as shown in Figure S2) do not shift in the spiral structures as the number of layers increases. The difference likely originates from a weak interlayer coupling when the twist angles between adjacent layers are small ($\sim 0.25^{\circ}$) as in spiral structures. Here, the approximate twist angle was taken from our previous study, where the structural information was obtained by both polarization-dependent SHG and transmission electron microscopy (TEM) measurements.²³ The exciton peak positions of spiral WS₂ can hence be used for reference and comparison with the SHG measurements.

To explore the dependence of SHG signal on the laser excitation wavelength λ_{in} , measurements were performed by tuning the laser excitation wavelength λ_{in} from 1150 to 1330 nm. Figure 3a inset shows the optical images of the light spot incident onto the samples, obtained from the charge-coupled device (CCD) camera at three representative emission wavelengths of λ_{out} = 400 nm, purple color (λ_{in} = 800 nm); 500 nm, green color (λ_{in} = 1000 nm); and 600 nm, red color $(\lambda_{in} = 1200 \text{ nm})$, which demonstrates the broad tunability of the SHG response. SHG signal spectra were measured by scanning the excitation wavelength λ_{in} from 1150 to 1330 nm with constant laser power (Figure 3a), which covers the A exciton (~640 nm) as shown in Figure 2b with a peak SHG signal appearing at 625 nm close to the A exciton position, 12,19 indicating a close relationship between SHG intensity and excitonic effects. Because there is another gradual intensity enhancement that cannot be attributed to A exciton close to 1150 nm, we further explored the short wavelength region in detail.

To study the behavior of SHG over a wider spectral range, the SHG intensity as a function of the excitation wavelength (780 to 1330 nm) was plotted in Figure 3b (see Figure S3 for detailed SHG spectra). In addition to the region near the A exciton (625 nm) discussed above, resonances at 500, 440, and 415 nm were also observed. These four SHG signal peaks match the A, B, C, and D excitons as observed in the linear reflectance spectra (Figure 2b). The peaks at ~625 and ~500 nm correspond to the A and B exciton states which result from the spin-orbit splitting of the valence band at the K point in the Brillouin zone (BZ).14 The measured energies of the excitons are very close to the A and B exciton states of monolayer WS2, suggesting a weak interlayer coupling and similarity between the electronic properties of our spiral flake and monolayer system. The measured SHG signal in the spiral flakes, however, displays a much large enhancement near the A and B excitons, while both peak intensities are significantly enhanced in comparison to the previously reported data for few-layer MoS_2 and WS_2 (~30 times). This observation



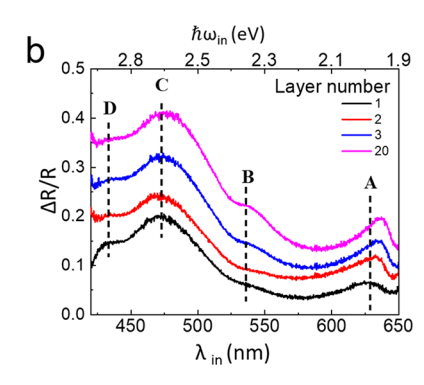
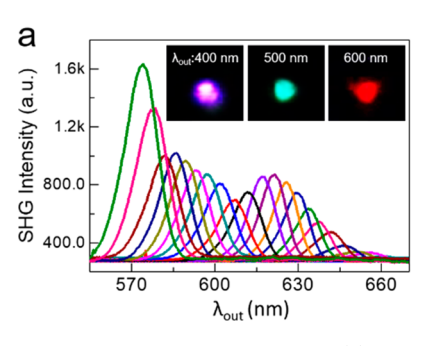


Figure 2. Results of nonlinear and linear optical measurements on a spiral WS_2 structure. (a) Second harmonic generation (SHG) signals under different laser power densities. (inset) The log scale plot of the SHG intensity with increasing laser power density. (b) Linear reflectance spectra of spiral WS_2 measured at spots with different layer numbers in the range of 400–650 nm.



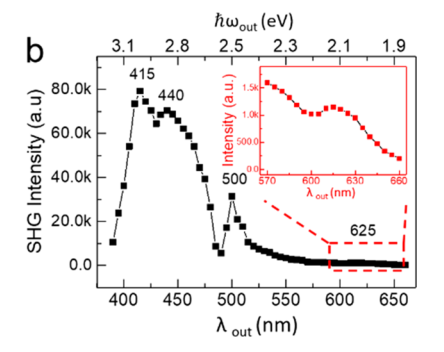


Figure 3. The SHG emission intensity spectrum of spiral WS₂. (a) SHG emission spectra of spiral WS₂ with the scanned excitation wavelength $\lambda_{\rm in}$ varying from 780 to 1330 nm. (inset) The optical images of spiral WS₂ illuminated by various $\lambda_{\rm in}$ (800, 1000, and 1200 nm) ($\lambda_{\rm out}$ = 400 nm, purple color; 500 nm, green color; and 600 nm, red color). (b) The SHG intensity as a function of the excitation energy. (inset) The magnification of local details near A exciton.

demonstrates the high SHG conversion efficiencies in spiral flakes compared to few layered samples (discussed later). Furthermore, an over 2 orders of magnitude enhancement of the SHG intensity on spiral WS₂ was observed when the excitation laser excitation energy was close to the energies of the C and D excitons states, but it shows much broader features in comparison to SHG signals resonant with A and B excitons. This is a surprising result since in TMDs SHG signal enhancements are in general reported from A and B excitons SHG and not from wavelengths near or above their bulk band gaps.

To explain the broadband enhancement behavior in WS₂

spiral structures far away from A and B excitons, theoretical calculations of the SHG susceptibility were carried out. First, as the basic unit of spiral structures, monolayer WS₂ belongs to the symmetry group D_{3h}, and its second-order susceptibility tensor has nonzero elemen $\chi_{y_1y_2y_3}^{(2)} = -\chi_{y_1x_2x_3}^{(2)} = -\chi_{x_1x_2y_3}^{(2)} = -\chi_{x_2x_2y_3}^{(2)} = -\chi_{x_2x_2y_3}^{(2)} = -\chi_{x_2x_2y_3}^{(2)}$ elements where x'y'z' are crystal coordinates and y' is along the zigzag direction. When a linearly polarized light (x is the polarization axis of the incident light) is incident along the -z' direction in the laboratory frame (xyz), the parallel (along x) and perpendicular (along y) SHG fields should be proportional to $\sin(3\varphi)$ and $\cos(3\varphi)$, respectively, where φ is the angle between x and x' axes and the total power collected in the experiment is independent of angle φ . For a spiral structure, the in-plane mirror symmetry of monolayer system would be broken by the special stacking sequence. Other symmetry breaking effects at the edges are not considered here, since as

reported previously by us, through comparison of SHG signals from both twisted and nontwisted samples, the contribution from edge states was found to be small in comparison to the bulk in twisted systems.^{23,34} This is because in a twisted sample, due to continuous symmetry breaking in the bulk and also owing to the large density of bulk states, the SHG signals are found to be not dominated by the edges. A phenomenological interpretation of the second harmonic response from spiral flakes, which can be regarded as a stack of many smallangle twisted layers, would be an interference of SHG signal from each layer. Assuming the system has N layers, the output electric field from each layer has the same amplitude $|E_{2\omega}|$, and the twisting angle between a pair of nearest layers n and n + 1is θ_n ; then, the total field can be written as a vector superposition, $E_{\text{spiral},2\omega} = E_{1\text{stlayer},2\omega} + E_{2\text{ndlayer},2\omega} + ... +$ $E_{Nthlaver,2\omega}$, with vectors from the first and the last layers forming a $3(\theta_1 + \theta_2 + ... + \theta_{N-1})$ angle (the total angle is around 15–20° in our system²³). Then, the SHG intensity could be written as $I_{2\omega,\text{spiral}} = (E_{2\omega} + E_{2\omega} \cos(3\theta_1) + ... + E_{2\omega} \cos(3(\theta_1 + \theta_2 + ... + \theta_{N-1})))^2 + (E_{2\omega} \sin(3\theta_1) + E_{2\omega} \sin(3(\theta_1 + \theta_2 + ... + \theta_{N-1})))^2 + (E_{2\omega} \sin(3\theta_1) + E_{2\omega} \sin(3(\theta_1 + \theta_2 + ... + \theta_{N-1})))^2 + (E_{2\omega} \sin(3\theta_1) + E_{2\omega} \sin(3(\theta_1 + \theta_2 + ... + \theta_{N-1})))^2 + (E_{2\omega} \sin(3\theta_1) + E_{2\omega} \sin(3(\theta_1 + \theta_2 + ... + \theta_{N-1})))^2 + (E_{2\omega} \sin(3\theta_1) + E_{2\omega} \sin(3(\theta_1 + \theta_2 + ... + \theta_{N-1})))^2 + (E_{2\omega} \sin(3\theta_1) + E_{2\omega} \sin(3(\theta_1 + \theta_2 + ... + \theta_{N-1})))^2 + (E_{2\omega} \sin(3(\theta_1 + \theta_2 + ... + \theta_{N-1})))^2 + (E_{2\omega} \sin(3(\theta_1 + \theta_2 + ... + \theta_{N-1})))^2 + (E_{2\omega} \sin(3(\theta_1 + \theta_2 + ... + \theta_{N-1})))^2 + (E_{2\omega} \sin(3(\theta_1 + \theta_2 + ... + \theta_{N-1})))^2 + (E_{2\omega} \sin(3(\theta_1 + \theta_2 + ... + \theta_{N-1})))^2 + (E_{2\omega} \sin(3(\theta_1 + \theta_2 + ... + \theta_{N-1})))^2 + (E_{2\omega} \sin(3(\theta_1 + \theta_2 + ... + \theta_{N-1})))^2 + (E_{2\omega} \sin(3(\theta_1 + \theta_2 + ... + \theta_{N-1})))^2 + (E_{2\omega} \sin(3(\theta_1 + \theta_2 + ... + \theta_{N-1})))^2 + (E_{2\omega} \sin(3(\theta_1 + \theta_2 + ... + \theta_{N-1})))^2 + (E_{2\omega} \sin(3(\theta_1 + \theta_2 + ... + \theta_{N-1})))^2 + (E_{2\omega} \sin(3(\theta_1 + \theta_2 + ... + \theta_{N-1})))^2 + (E_{2\omega} \cos(3(\theta_1 + \theta_2 + ... + \theta_{N-1})))^2 + (E_{2\omega} \cos(3(\theta_1 + \theta_2 + ... + \theta_{N-1})))^2 + (E_{2\omega} \cos(3(\theta_1 + \theta_2 + ... + \theta_N))^2 + (E_{2\omega} \cos(3(\theta_1 + \theta_2 + ... + \theta_N))^2 + (E_{2\omega} \cos(3(\theta_1 + \theta_2 + ... + \theta_N))^2 + (E_{2\omega} \cos(3(\theta_1 + \theta_2 + ... + \theta_N))^2 + (E_{2\omega} \cos(3(\theta_1 + \theta_2 + ... + \theta_N))^2 + (E_{2\omega} \cos(3(\theta_1 + \theta_2 + ... + \theta_N))^2 + (E_{2\omega} \cos(3(\theta_1 + \theta_2 + ... + \theta_N))^2 + (E_{2\omega} \cos(3(\theta_1 + ... + \theta_N))^2 +$ (θ_2)) + ... + $(E_{2\omega})\sin(3(\theta_1 + \theta_2 + ... + \theta_{N-1}))^2$. This expression shows that the total SHG intensity would increase with increasing layer numbers and explains the large nonlinear optical conversion efficiency in spiral flakes in comparison to a monolayer system. Furthermore, in the weak interlayer coupling limit (as also indicated by the similar reflectance spectra (Figure 2b) and PL spectra (Figure S2) measured in regions with different layer numbers from the spiral WS₂ flake), characteristics of SHG signal in a spiral flake should follow that of a monolayer. This is in accordance with previous studies

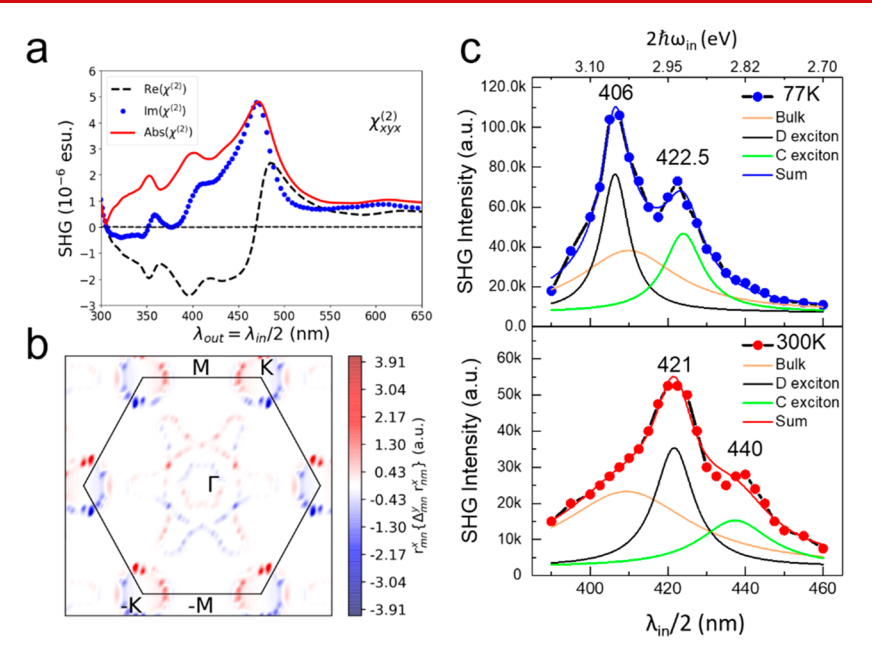


Figure 4. First-principles calculated SHG signals in single-electron approximation and experimentally measured SHG from spiral WS₂ with varying temperatures and laser excitation energies. (a) The SHG susceptibility of WS₂, $\chi_{xyz}^{(2)} = \chi^{(2)}$, as a function of excitation energy $\hbar\omega_{in}$ from the first-principles calculation. (b) The Brillouin zone distribution of the integrand $r_{nm}^x \{\Delta_{mn}^y r_{nm}^x\}$ in eq 1 at excitation energy $\hbar\omega = 1.35$ eV, from first-principles calculation, showing enhancements near Γand K points. (c) SHG data with an emission wavelength λ_{out} ranging from 390 to 460 nm, measured at 77 and 300 K with fixed laser power. Three Lorentz fitting curves are denoted by green, black, and orange lines.

that the interlayer coupling strength in multilayer TMD systems is smaller when a twist angle exists. Therefore, we will first calculate $\chi^{(2)}$ of monolayer WS₂ to compare with the experimental results and then briefly discuss extensions to the spiral case along with some discrepancies between the theory and experiments.

In our measurements, the excitation energy corresponding to excitation wavelength $\lambda_{\rm in}$ of incident light, ranging from 780 to 920 nm, was always larger than half of the bandgap while smaller than the smallest exciton energy and also the full bandgap of WS₂ ($\frac{E_g}{2} < \hbar\omega_{\rm in} < E_{\rm ex} < E_g$, where E_g is the bandgap and $E_{\rm ex}$ is the smallest exciton energy, so that interband transitions with $E_m - E_n \sim \hbar\omega$ (E_m is the energy eigenvalue of band m) resonances are negligible, while dominating terms are with $E_m - E_n \sim 2\hbar\omega$ resonances. Then, the microscopic expression of the main contribution to SHG susceptibility can be written as (based on Hugh and Sipe's derivation 36):

$$\chi^{abc}(-2\omega, \omega, \omega) = \frac{e^3}{\hbar^2} \int_{BZ} \frac{d\mathbf{k}}{V} \left\{ \sum_{n,m} -8ir_{nm}^a \{ \Delta_{mn}^b r_{mn}^c \} \frac{1}{\omega_{mn}^2} \frac{f_{nm}}{(\omega_{mn} - 2\omega)} + \sum_{n,m,l} r_{nm}^a \{ r_{ml}^b r_{ln}^c \} \left\{ \frac{1}{\omega_{ln} - \omega_{ml}} + \frac{(\omega_{ml} - \omega_{ln})}{\omega_{mn}^2} \right\} \frac{2f_{nm}}{(\omega_{mn} - 2\omega)} \right\}$$
(1)

where f_{nm} is the Fermi–Dirac distribution; the matrix elements of the velocity operator acting on Bloch states are given by $\mathbf{v}_{nm}(\mathbf{k}) = \langle u_n(\mathbf{k})|\mathbf{v}|u_m(\mathbf{k})\rangle$, and $\mathbf{\Delta}_{nm}$ is defined by $\mathbf{v}_{nn} - \mathbf{v}_{mm} \cdot \mathbf{r}_{nm}(\mathbf{k})$ which is the interband matrix element of the position operator (or interband Berry connection), and $\mathbf{r}_{nm}(\mathbf{k}) = \frac{\mathbf{v}_{mm}(\mathbf{k})}{i(\epsilon_n(\mathbf{k}) - \epsilon_m(\mathbf{k}))}$ for $n \neq m$. Different from the explanation for the large linear optical conductivities at some specific energies within the bulk bands in TMD systems 37,38 where high density of states at van Hove singularities (band

saddling points) was the primary cause, SHG as a nonlinear optical process involves both interband and intraband processes and cannot be directly related to the distribution of the density of states. The integrand in the response function (eq 1) indicates that the SHG susceptibility is very closely associated with the interband Berry connection between the conduction bands and valence bands.

In order to extract microscopic information from this system, we used first-principle calculations based on the full band structure of monolayer WS2 to evaluate eq 1 under the single-electron approximation (see equations of full contributions for SHG in the Supporting Information). The susceptibility tensor element $\chi_{xyz}^{(2)}$ of WS₂ (the only independent term responsible for the measured signal) was calculated as a function of the excitation energy $(\hbar\omega_{in})$, as shown in Figure 4a. It displays a wide and strong resonance peak at ~460 nm which qualitatively reproduces the experimentally observed broad enhancement above the quasiparticle band gap. The slight discrepancies in peak positions likely originate from the many-body effects including electron self-interactions and electron-hole interactions, which are not accounted for in our model. 39,40 By comparing the enhancement peak position with the possible transition energies in the band structure, it can be seen that the large SHG susceptibility peak is related to the regions near the Γ -K line in the Brillouin zone. To further quantify this argument, the integrand $(r_{nm}^x \{\Delta_{mn}^y r_{nm}^x\})$ in eq 1 (momentum-resolved SHG susceptibility) corresponding to the interband transitions at the peak position $\lambda_{in}/2 = 460$ nm was plotted in the Brillouin zone, as shown in Figure 4b. Again, the integrand is prominent in the regions near Γ and K points, and this correspondence indicates that a large SHG signal can be related to the bulk interband Berry connection properties when two bands are in resonance with the excitation energy. If we further take into consideration the interlayer coupling, then a

difference due to the spiral structure would result in a more nested band structure due to Brillouin zone folding⁴¹ and, consequently, its SHG may be further enhanced in the higher energy flat band regions, making them favorable for generating large nonlinear optical responses above the bandgap. Although the discussion here is not based on the full electronic structure of the spiral structure, the experimentally measured enhancement of SHG above the bandgap in the spiral structure could still be qualitatively reproduced by first-principles calculations for a monolayer structure, presumably due to the weak interlayer coupling strength. More importantly, the correspondence between certain regions in the Brillouin zone where interband Berry connections are large to the broad and strong SHG signals we observed experimentally demonstrates the contributions from a large interband Berry connection in the system, and we envision that this argument could be applied to other nonlinear optical systems.

In addition to bulk band contributions, the excitonic contribution was experimentally verified by temperaturedependent SHG measurements. Figure 4c shows the SHG intensities measured with fixed laser power, under various excitation wavelengths λ_{in} at 77 and 300 K (see Figure S4 for original spectra). The positions of two SHG peaks near the C and D excitons were located at 421 and 440 nm at 300 K, similar to the peak positions of 433 and 470 nm obtained by linear reflectance spectra in Figure 2b. The wavelength dependence data of SHG measured from spiral WS2 were fitted by three Lorentzian functions; the black and green curves correspond to D and C excitons. The orange curve corresponds to the "bulk" contribution whose peak position and shape does not change with temperature. The fitting curves show that at 77 K, the C and D excitonic peaks show blue shifts of ~17 and 15 nm, respectively, and both peaks became stronger and narrower, confirming their excitonic behavior. These two excitonic resonances could be well explained by the high responsivity of the unbounded exciton levels in the excitonic basis. 42 Furthermore, the orange peak from the bulk contribution, which centers at ~410 nm, is much broader than the excitonic peaks but has a comparable weight. This peak corresponds to the energy region where large interband Berry connections contribute to on-resonance optical transitions and, hence, large momentum-resolved SHG susceptibilities. Therefore, both the C and D excitonic resonances and Berry connection properties gave rise to the giant SHG enhancement far away from the widely explored A and B excitons in previous studies.

In conclusion, we have systemically measured the wavelength- and temperature-dependent SHG of a spiral WS2 structure across a large spectral range from A to D excitons and into the bulk bandgap. Strong SHG signals were observed with excitation wavelengths ranging from 780 to 1330 nm, and an over 2 orders of magnitude enhancement of SHG amplitude is observed near the UV region. The huge SHG enhancement originates from not only C and D exciton resonances but also due to the resonance of large interband Berry connections contributing to certain transitions within the high energy spectral regime. The spiral structure is a multilayer generalization from twisted bilayer structures, whose Moiré excitons have generated widespread interest in the domain of linear optics. Our work showing the strong SHG signal efficiency of spiral TMD in the nonlinear optics domain and its connection to intrinsic band properties is promising for nonlinear optical studies of "twistronic" systems in general and could also be

utilized for designing efficient SHG crystals over a broad range of wavelengths and their potential applications as novel nonlinear media for device applications.⁴³

METHODS

Sample Preparation. To prepare spiral structures on quartz substrates for SHG measurements, spiral structures grown on Si substrates (with 300 nm of $\mathrm{SiO_2}$) were first spin-coated with PMMA (A4), leaving an ~100 nm thick polymer film. After being cured at 100 °C for 15 min, the PMMA/WS₂ sample was detached from the $\mathrm{Si/SiO_2}$ substrate with 30% KOH solution. Then, the sample was transferred with deionized (DI) water to reduce the KOH residue. Afterward, the PMMA/WS₂ membrane was transferred onto a quartz substrate, followed by the removal of PMMA film using acetone. Finally, the sample was cleaned by isopropyl alcohol and deionized water.

Sample Characterization. (1) The samples are characterized by optical microscopy (OM, Zeiss Axio Imager A1) and atomic force microscopy (AFM Bruker Multimode 8).

- (2) Reflection spectra were taken by our home-built system with a tungsten-halogen lamp used as the light source. The broadband light was focused to a ~2 μ m spot on the sample surface and the reflected beam was measured by a spectrometer. The reflected signals were collected both from the spiral sample area ($R_{\rm inside}$) and from the substrate ($R_{\rm outside}$), and the reflectance was subsequently calculated by $\Delta R/R = (R_{\rm outside} R_{\rm inside})/R_{\rm outside}$.
- (3) Transmission mode SHG measurements were performed using a confocal microscope (WITec, alpha-300). A mode-locked Ti/sapphire laser (Tsunami) at 800 nm (pulse width 80 fs, repetition frequency 80 MHz) was amplified by a regenerative amplifier laser (Spitfire Ace 100, 1 kHz) and then was introduced into an optical parameter amplifier (OPA, TOPAS Prime). The output laser from the OPA can be continuously tuned from 780 to 1330 nm and used for the SHG measurements. The source light was focused by an infrared objective lens (10×, Zeiss) from the bottom to the sample. The SHG signal was collected by another objective lens (20×, Zeiss), while the light source was filtered by an optical filter and the SHG signal passed.

For reflection mode SHG measurements we used a 140 fs Ti/sapphire oscillator (Coherent Chameleon) with 80 MHz repetition and a tunable wavelength from 680 to 1080 nm. The SHG measurements at room temperature were obtained using a 60× objective lens, whereas variable-temperature SHG measurements were performed using a home-built, low-temperature microscopy system. The back-reflected signal was then directed to a dichroic and a thin bandpass centered at the SHG wavelength to completely remove the laser scattered light, and the SHG signal was detected by a spectrometer.

First-principles DFT Calculation Details. First-principles DFT calculations were mainly performed with the Vienna Ab Initio Simulation Package(VASP)⁴⁴ using the projector augmented wave method⁴⁵ and the plane-wave basis with an energy cutoff of 500 eV. The Perdew–Burke–Ernzerhof (PBE) exchange-correlation functional⁴⁶ was used. The structural optimization calculations were performed with a force criterion of 0.01 eV/ $^{\circ}$ A. The Monkhorst–Pack k-point meshes of $10 \times 10 \times 1$ were adopted for the calculations of monolayer structures. For nonlinear optical response calculation, we used the Monkhorst–Pack k-point meshes of $64 \times 64 \times 1$. The k-point meshes of $72 \times 72 \times 1$ were used to test

the convergence of the current and second-harmonic generation. Since we used the sum rule to calculate the two-photon vertex, a bunch of unoccupied bands are needed to get converged results. We used 200 valence bands to calculate the second-order optical response, and 300 valence bands were used to test the convergence.

ASSOCIATED CONTENT

Solution Supporting Information

The Supporting Information is available free of charge at https://pubs.acs.org/doi/10.1021/acs.nanolett.0c00305.

Calculation of the second harmonic generation susceptibility tensor; AFM characterization, linear optical emission, and detailed wavelength-dependent SHG signals of spiral WS_2 samples (PDF)

AUTHOR INFORMATION

Corresponding Authors

Ritesh Agarwal — Department of Materials Science and Engineering, University of Pennsylvania, Philadelphia, Pennsylvania 19104, United States; ⊚ orcid.org/0000-0002-1289-4334; Email: riteshag@seas.upenn.edu

Anlian Pan — Key Laboratory for Micro-Nano Physics and Technology of Hunan Province, State Key Laboratory of Chemo/Biosensing and Chemometrics, and College of Materials Science and Engineering, Hunan University, Changsha 410082, China; ⊙ orcid.org/0000-0003-3335-3067; Email: anlian.pan@hnu.edu.cn

Authors

Xiaopeng Fan — Key Laboratory for Micro-Nano Physics and Technology of Hunan Province, State Key Laboratory of Chemo/Biosensing and Chemometrics, and College of Materials Science and Engineering, Hunan University, Changsha 410082, China; Department of Materials Science and Engineering, University of Pennsylvania, Philadelphia, Pennsylvania 19104, United States

Zhurun Ji — Department of Materials Science and Engineering, University of Pennsylvania, Philadelphia, Pennsylvania 19104, United States

Ruixiang Fei – Department of Physics, Washington University in St. Louis, St. Louis, Missouri 63130, United States

Weihao Zheng — Key Laboratory for Micro-Nano Physics and Technology of Hunan Province, State Key Laboratory of Chemo/Biosensing and Chemometrics, and College of Materials Science and Engineering, Hunan University, Changsha 410082, China

Wenjing Liu — Department of Materials Science and Engineering, University of Pennsylvania, Philadelphia, Pennsylvania 19104, United States; ◎ orcid.org/0000-0002-9441-8859

Xiaoli Zhu — Key Laboratory for Micro-Nano Physics and Technology of Hunan Province, State Key Laboratory of Chemo/Biosensing and Chemometrics, and College of Materials Science and Engineering, Hunan University, Changsha 410082, China

Shula Chen — Key Laboratory for Micro-Nano Physics and Technology of Hunan Province, State Key Laboratory of Chemo/Biosensing and Chemometrics, and College of Materials Science and Engineering, Hunan University, Changsha 410082, China Li Yang — Department of Physics, Washington University in St. Louis, St. Louis, Missouri 63130, United States

Hongjun Liu — Institute of Functional Crystals, Tianjing University of Technology, Tianjin 300384, China; orcid.org/0000-0002-6656-2669

Complete contact information is available at: https://pubs.acs.org/10.1021/acs.nanolett.0c00305

Author Contributions

¹X.F. and Z.J. contributed equally.

Notes

The authors declare no competing financial interest.

ACKNOWLEDGMENTS

A.P. is supported by the National Natural Science Foundation of China (51525202 and U19A2090.) R.A. acknowledges the support from the U.S. Army Research Office (grant no. W911NF-17-1-0436), Office of Naval Research MURI (grant no. N00014-17-1-2661), and the NSF-QII-TAQS (no. 1936276) grant from the NSF (USA). R.F. and L.Y. are supported by the National Science Foundation (NSF) CAREER grant DMR-1455346 and the Air Force Office of Scientific Research (AFOSR) grant FA9550-17-1-0304. The computational resources have been provided by the Stampede of TeraGrid at the Texas Advanced Computing Center (TACC) through XSEDE.

REFERENCES

- (1) Franken, P. A.; Hill, A. E.; Peters, C. W.; Weinreich, G. Generation of Optical Harmonics. *Phys. Rev. Lett.* **1961**, 7 (4), 118–119
- (2) Campagnola, P. J.; Loew, L. M. Second-harmonic imaging microscopy for visualizing biomolecular arrays in cells, tissues and organisms. *Nat. Biotechnol.* **2003**, *21* (11), 1356–60.
- (3) Shen, Y. R. The Principles of Nonlinear Optics; J. Wiley & Sons Inc.: Hoboken, NJ, 2003.
- (4) Ren, M. L.; Agarwal, R.; Liu, W.; Agarwal, R. Crystallographic Characterization of II-VI Semiconducting Nanostructures via Optical Second Harmonic Generation. *Nano Lett.* **2015**, *15* (11), 7341–7346.
- (5) Eisenthal, K. B. Liquid Interfaces Probed by Second-Harmonic and Sum-Frequency Spectroscopy. *Chem. Rev.* **1996**, *96*, 1343–1360.
- (6) Fejer, M. M.; Magel, G. A.; Jundt, D. H.; Byer, R. L. Quasi-phase-matched second harmonic generation: tuning and tolerances. *IEEE J. Quantum Electron.* **1992**, 28, 2631–2654.
- (7) Ren, M. L.; Liu, W.; Aspetti, C. O.; Sun, L.; Agarwal, R. Enhanced second-harmonic generation from metal-integrated semi-conductor nanowires via highly confined whispering gallery modes. *Nat. Commun.* **2014**, *5*, 5432.
- (8) Mak, K. F.; Lee, C.; Hone, J.; Shan, J.; Heinz, T. F. Atomically thin MoS₂: a new direct-gap semiconductor. *Phys. Rev. Lett.* **2010**, *105* (13), 136805.
- (9) Fan, X.; Zheng, W.; Liu, H.; Zhuang, X.; Fan, P.; Gong, Y.; Li, H.; Wu, X.; Jiang, Y.; Zhu, X.; Zhang, Q.; Zhou, H.; Hu, W.; Wang, X.; Duan, X.; Pan, A. Nonlinear photoluminescence in monolayer WS₂: parabolic emission and excitation fluence-dependent recombination dynamics. *Nanoscale* **2017**, *9* (21), 7235–7241.
- (10) Lucking, M. C.; Beach, K.; Terrones, H. Large second harmonic generation in alloyed TMDs and boron nitride nanostructures. *Sci. Rep.* **2018**, *8* (1), 10118.
- (11) Saynatjoki, A.; Karvonen, L.; Rostami, H.; Autere, A.; Mehravar, S.; Lombardo, A.; Norwood, R. A.; Hasan, T.; Peyghambarian, N.; Lipsanen, H.; Kieu, K.; Ferrari, A. C.; Polini, M.; Sun, Z. Ultra-strong nonlinear optical processes and trigonal warping in MoS₂ layers. *Nat. Commun.* **2017**, 8 (1), 893.

- (12) Zeng, Z.; Sun, X.; Zhang, D.; Zheng, W.; Fan, X.; He, M.; Xu, T.; Sun, L.; Wang, X.; Pan, A. Controlled Vapor Growth and Nonlinear Optical Applications of Large-Area 3R Phase WS₂ and WSe, Atomic Layers. *Adv. Funct. Mater.* **2019**, 29 (11), 1806874.
- (13) Zhang, L.; Liu, K.; Wong, A. B.; Kim, J.; Hong, X.; Liu, C.; Cao, T.; Louie, S. G.; Wang, F.; Yang, P. Three-dimensional spirals of atomic layered MoS₂. *Nano Lett.* **2014**, *14* (11), 6418–23.
- (14) Zhao, M.; Ye, Z.; Suzuki, R.; Ye, Y.; Zhu, H.; Xiao, J.; Wang, Y.; Iwasa, Y.; Zhang, X. Atomically phase-matched second-harmonic generation in a 2D crystal. *Light: Sci. Appl.* **2016**, *5* (8), No. e16131.
- (15) Janisch, C.; Wang, Y.; Ma, D.; Mehta, N.; Elias, A. L.; Perea-Lopez, N.; Terrones, M.; Crespi, V.; Liu, Z. Extraordinary Second Harmonic Generation in tungsten disulfide monolayers. *Sci. Rep.* **2015**, *4*, 5530.
- (16) Lin, K. I.; Ho, Y. H.; Liu, S. B.; Ciou, J. J.; Huang, B. T.; Chen, C.; Chang, H. C.; Tu, C. L.; Chen, C. H. Atom-Dependent Edge-Enhanced Second-Harmonic Generation on MoS₂ Monolayers. *Nano Lett.* **2018**, *18* (2), 793–797.
- (17) Yin, X. B.; Ye, Z. L.; Chenet, D. A.; Ye, Y.; O'Brien, K.; Hone, J. C.; Zhang, X. Edge Nonlinear Optics on a MoS₂ Atomic Monolayer. *Science* **2014**, 344, 488–490.
- (18) Zhang, Y.; Huang, D.; Shan, Y.; Jiang, T.; Zhang, Z.; Liu, K.; Shi, L.; Cheng, J.; Sipe, J. E.; Liu, W. T.; Wu, S. Doping-Induced Second-Harmonic Generation in Centrosymmetric Graphene from Quadrupole Response. *Phys. Rev. Lett.* **2019**, 122 (4), 047401.
- (19) Zeng, H.; Liu, G. B.; Dai, J.; Yan, Y.; Zhu, B.; He, R.; Xie, L.; Xu, S.; Chen, X.; Yao, W.; Cui, X. Optical signature of symmetry variations and spin-valley coupling in atomically thin tungsten dichalcogenides. *Sci. Rep.* **2013**, *3*, 1608.
- (20) Lin, X.; Liu, Y.; Wang, K.; Wei, C.; Zhang, W.; Yan, Y.; Li, Y. J.; Yao, J.; Zhao, Y. S. Two-Dimensional Pyramid-like WS₂ Layered Structures for Highly Efficient Edge Second-Harmonic Generation. *ACS Nano* **2018**, *12* (1), 689–696.
- (21) Yu, H.; Talukdar, D.; Xu, W.; Khurgin, J. B.; Xiong, Q. Charge-Induced Second-Harmonic Generation in Bilayer WSe₂. *Nano Lett.* **2015**, *15* (8), 5653–7.
- (22) Hsu, W. T.; Zhao, Z. A.; Li, L. J.; Chen, C. H.; Chiu, M. H.; Chang, P. S.; Chou, Y. C.; Chang, W. H. Second Harmonic Generation from Artificially Stacked Transition Metal Dichalcogenide Twisted Bilayers. ACS Nano 2014, 8 (3), 2951–2958.
- (23) Fan, X.; Jiang, Y.; Zhuang, X.; Liu, H.; Xu, T.; Zheng, W.; Fan, P.; Li, H.; Wu, X.; Zhu, X.; Zhang, Q.; Zhou, H.; Hu, W.; Wang, X.; Sun, L.; Duan, X.; Pan, A. Broken Symmetry Induced Strong Nonlinear Optical Effects in Spiral WS₂ Nanosheets. *ACS Nano* **2017**, *11* (5), 4892–4898.
- (24) Fan, X.; Zhao, Y.; Zheng, W.; Li, H.; Wu, X.; Hu, X.; Zhang, X.; Zhu, X.; Zhang, Q.; Wang, X.; Yang, B.; Chen, J.; Jin, S.; Pan, A. Controllable Growth and Formation Mechanisms of Dislocated WS₂ Spirals. *Nano Lett.* **2018**, *18* (6), 3885–3892.
- (25) Wang, G.; Marie, X.; Gerber, I.; Amand, T.; Lagarde, D.; Bouet, L.; Vidal, M.; Balocchi, A.; Urbaszek, B. Giant enhancement of the optical second-harmonic emission of WSe₂ monolayers by laser excitation at exciton resonances. *Phys. Rev. Lett.* **2015**, *114* (9), 097403.
- (26) Malard, L. M.; Alencar, T. V.; Barboza, A. P. M.; Mak, K. F.; de Paula, A. M. Observation of intense second harmonic generation from MoS₂ atomic crystals. *Phys. Rev. B: Condens. Matter Mater. Phys.* **2013**, 87 (20), 201401.
- (27) Sun, J.; Gu, Y.-J.; Lei, D. Y.; Lau, S. P.; Wong, W.-T.; Wong, K.-Y.; Chan, H. L.-W. Mechanistic Understanding of Excitation-Correlated Nonlinear Optical Properties in MoS₂ Nanosheets and Nanodots: The Role of Exciton Resonance. *ACS Photonics* **2016**, 3 (12), 2434–2444.
- (28) Zhao, W.; Ribeiro, R. M.; Toh, M.; Carvalho, A.; Kloc, C.; Castro Neto, A. H.; Eda, G. Origin of indirect optical transitions in few-layer MoS₂, WS₂, and WSe₂. *Nano Lett.* **2013**, *13* (11), 5627–34. (29) Wang, D.; Zhang, X.; Liu, H.; Meng, J.; Xia, J.; Yin, Z.; Wang, Y.; You, J.; Meng, X.-M. Epitaxial growth of HfS₂ on sapphire by

- chemical vapor deposition and application for photodetectors. 2D Mater. 2017, 4 (3), 031012.
- (30) Zhang, X. Q.; Lin, C. H.; Tseng, Y. W.; Huang, K. H.; Lee, Y. H. Synthesis of lateral heterostructures of semiconducting atomic layers. *Nano Lett.* **2015**, *15* (1), 410–5.
- (31) Zhou, J.; Lin, J.; Huang, X.; Zhou, Y.; Chen, Y.; Xia, J.; Wang, H.; Xie, Y.; Yu, H.; Lei, J.; Wu, D.; Liu, F.; Fu, Q.; Zeng, Q.; Hsu, C. H.; Yang, C.; Lu, L.; Yu, T.; Shen, Z.; Lin, H.; Yakobson, B. I.; Liu, Q.; Suenaga, K.; Liu, G.; Liu, Z. A library of atomically thin metal chalcogenides. *Nature* **2018**, *556* (7701), 355–359.
- (32) Li, Y.; Chernikov, A.; Zhang, X.; Rigosi, A.; Hill, H. M.; van der Zande, A. M.; Chenet, D. A.; Shih, E.-M.; Hone, J.; Heinz, T. F. Measurement of the optical dielectric function of monolayer transition-metal dichalcogenides:MoS₂, MoSe₂, WS₂, and WSe₂. Phys. Rev. B: Condens. Matter Mater. Phys. **2014**, 90 (20), 205422.
- (33) Zhao, W. J.; Ghorannevis, Z.; Chu, L. Q.; Toh, M. L.; Kloc, C.; Tan, P. H.; Eda, G. Evolution of Electronic Structure in Atomically Thin Sheets of WS₂ and WSe₂. ACS Nano **2013**, 7 (1), 791–797.
- (34) Shearer, M. J.; Samad, L.; Zhang, Y.; Zhao, Y.; Puretzky, A.; Eliceiri, K. W.; Wright, J. C.; Hamers, R. J.; Jin, S. Complex and noncentrosymmetric stacking of layered metal dichalcogenice materials created by screw dislocations. *J. Am. Chem. Soc.* **2017**, *139* (9), 3496–3504.
- (35) Liu, K.; Zhang, L.; Cao, T.; Jin, C.; Qiu, D.; Zhou, Q.; Zettl, A.; Yang, P.; Louie, S. G.; Wang, F. Evolution of interlayer coupling in twisted molybdenum disulfide bilayers. *Nat. Commun.* **2014**, *5*, 4966.
- (36) Hughes, J. L.; Sipe, J. Calculation of second-order optical response in semiconductors. *Phys. Rev. B: Condens. Matter Mater. Phys.* **1996**, 53 (16), 10751.
- (37) Gibertini, M.; Pellegrino, F. M. D.; Marzari, N.; Polini, M. Spinresolved optical conductivity of two-dimensional group-VIB transition-metal dichalcogenides. *Phys. Rev. B: Condens. Matter Mater. Phys.* **2014**, *90* (24), 245411.
- (38) Carvalho, A.; Ribeiro, R. M.; Castro Neto, A. H. Band nesting and the optical response of two-dimensional semiconducting transition metal dichalcogenides. *Phys. Rev. B: Condens. Matter Mater. Phys.* **2013**, 88 (11), 115205.
- (39) Trolle, M. L.; Seifert, G.; Pedersen, T. G. Theory of excitonic second-harmonic generation in monolayerMoS₂. *Phys. Rev. B: Condens. Matter Mater. Phys.* **2014**, 89 (23), 235410.
- (40) Wang, L.; Wang, Z.; Wang, H. Y.; Grinblat, G.; Huang, Y. L.; Wang, D.; Ye, X. H.; Li, X. B.; Bao, Q.; Wee, A. S.; Maier, S. A.; Chen, Q. D.; Zhong, M. L.; Qiu, C. W.; Sun, H. B. Slow cooling and efficient extraction of C-exciton hot carriers in MoS₂ monolayer. *Nat. Commun.* **2017**, *8*, 13906.
- (41) Tan, Y.; Chen, F. W.; Ghosh, A. W. First principles study and empirical parametrization of twisted bilayer MoS_2 based on band-unfolding. *Appl. Phys. Lett.* **2016**, 109 (10), 101601.
- (42) Pedersen, T. G. Intraband effects in excitonic second-harmonic generation. *Phys. Rev. B: Condens. Matter Mater. Phys.* **2015**, 92, 235432.
- (43) Ren, M. L.; Berger, J. S.; Liu, W.; Liu, G.; Agarwal, R. Strong modulation of second-harmonic generation with very large contrast in semiconducting CdS via high-field domain. *Nat. Commun.* **2018**, 9 (1), 186.
- (44) Kresse, G.; Furthmüller, J. Efficient iterative schemes for ab initio total-energy calculations using a plane-wave basis set. *Phys. Rev. B: Condens. Matter Mater. Phys.* **1996**, *54*, 11169–11186.
- (45) Kresse, G.; Joubert, D. From ultrasoft pseudopotentials to the projector augmented-wave method. *Phys. Rev. B: Condens. Matter Mater. Phys.* **1999**, *59*, 1758–1775.
- (46) Perdew, J. P.; Burke, K.; Ernzerhof, M. Generalized Gradient Approximation Made Simple. *Phys. Rev. Lett.* **1996**, *77*, 3865–3868.